


Fully Packaged Multichannel Cryogenic Quantum Memory Module

David J. Starling^{1,*}, Katia Shtyrkova,¹ Ian Christen,² Ryan Murphy,¹ Linsen Li,² Kevin C. Chen,² Dave Kharas,¹ Xingyu Zhang,^{1,†} John Cummings,¹ W. John Nowak,¹ Eric Bersin,¹ Robert J. Niffenegger,^{1,‡} Madison Sutula,² Dirk Englund,² Scott Hamilton,¹ and P. Benjamin Dixon¹

¹*Lincoln Laboratory, Massachusetts Institute of Technology, Lexington, Massachusetts 02421, USA*

²*Research Laboratory of Electronics, Massachusetts Institute of Technology, Cambridge, Massachusetts 02139, USA*

 (Received 1 March 2023; revised 8 May 2023; accepted 12 May 2023; published 8 June 2023)

Realizing a quantum network will require long-lived quantum memories with optical interfaces incorporated into a scalable architecture. Color-center quantum emitters in diamond have emerged as a promising memory modality due to their optical properties and compatibility with scalable integration. However, developing a scalable color-center emitter module requires significant advances in the areas of heterogeneous integration and cryogenically compatible packaging. Here we report on a cryogenically stable and network compatible quantum emitter module for memory use. This quantum emitter module is a significant development towards advanced quantum networking applications such as distributed sensing and processing.

DOI: [10.1103/PhysRevApplied.19.064028](https://doi.org/10.1103/PhysRevApplied.19.064028)

I. INTRODUCTION

Quantum memory systems are a crucial enabling technology for the continued development and realization of advanced quantum network capabilities and applications [1]. Indeed, memory systems scaled to tens or hundreds of memories with millisecond-class coherence times would enable quantum repeater functionality [2,3] for improved network performance [4–7] and quantum network applications, such as improved sensing [8] and distributed quantum processing [9,10].

There are multiple candidate qubit platforms for networked quantum memory use, including trapped ions [11, 12] and neutral atoms [13,14], atomic ensembles in vapors [15,16] and in solid-state materials [17–19], and individual color centers in solids [20–22]. Diamond color-center emitters have emerged as a particularly promising platform due to several beneficial characteristics [23]. Their coherent optical interface provides compatibility with optical fiber networks [24,25]. They have the potential to scale to thousands of memory qubits through on-chip integration [26], and their electron-spin degree of freedom can exhibit coherence times ranging from milliseconds [27] to seconds [28], providing utility as quantum repeaters and for quantum network applications. Furthermore, ancillary nuclear spins can be used as logical registers [29] for multiqubit

processing, such as error detection [30] and correction [31]. However, the challenges of engineering a robust and scalable memory module has limited the use of these memories in network testbeds, delaying demonstration of advanced quantum network applications.

Here we report on our efforts to develop a robust, packaged quantum emitter module. We build upon previous work [26,32,33] to demonstrate heterogeneous integration of optical fibers, photonic integrated circuits (PICs), and diamond color centers. Our results rely upon alternative custom-designed and fabricated silicon-nitride (Si_3N_4 , SiN) PICs, matched diamond microchips with waveguides containing negatively charged silicon vacancy (Si-V^-) color centers, a custom diamond alignment and stamping process, as well as an alternative precision fiber alignment and bonding procedure. We follow the previously reported general strategy of multi-waveguide-fiber architecture [26,32,33] and incorporate our developments to realize a multiemitter module that is fully packaged, cryogenically compatible, inherently scalable, and network compatible. The resulting quantum emitter module architecture enables scaling of large numbers of optical quantum memories to be readily integrated into emerging network testbeds [34–36] for the realization of applications in quantum networking.

II. DESIGN AND DEVELOPMENT

The conceptual goal of our work is to develop a cryo-compatible, fully packaged module that interfaces optical

*David.Starling@ll.mit.edu

†Now at McKinsey & Company.

‡Now at University of Massachusetts, Amherst.

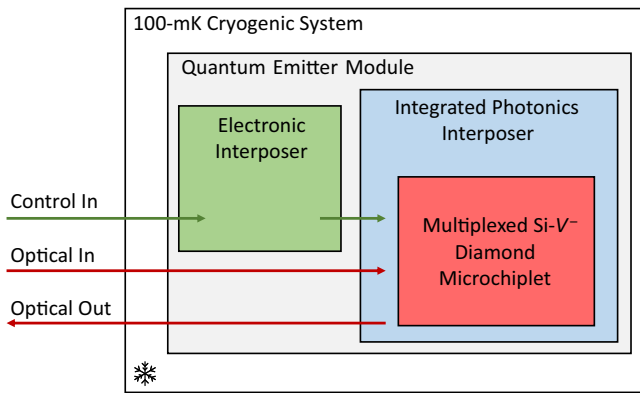


FIG. 1. Conceptual block diagram of the quantum emitter module. The module operates in a cryogenic environment. Electrical control signals are fed into the cryogenic system and routed via an electronic interposer that directs signals to an integrated photonics interposer that can interface with a multiplexed Si- V^- diamond microchiplet for qubit control. Optical signals are fed into the cryogenic system and routed via the same photonic interposer to enable optical interaction with the multiplexed Si- V^- diamond microchiplet.

fiber with a controllable quantum emitter, as shown in Fig. 1. To accomplish this task, our design uses a custom electronic interposer, an integrated photonic interposer (the PIC) and a diamond microchiplet—incorporated into a commercial dilution refrigerator. The electronic interposer is produced commercially, and the eight-channel diamond microchiplet is fabricated using a similar process to the one shown in Refs. [26,37,38] (see Appendix A for details). In what follows, we focus on the fabrication of the integrated photonic interposer and the packaging methodologies.

We design and fabricate a custom PIC interposer to integrate a commercial optical fiber array with a diamond microchiplet. This process has been accomplished previously in Ref. [26] using unclad aluminum nitride waveguides on a sapphire wafer where the waveguides were exposed (unclad) to allow for heterogeneous integration. However, the small optical mode in the unclad aluminum nitride waveguide at the facet necessitated the use of lensed and/or high numerical aperture fiber to obtain efficient coupling. Additionally, it is possible to use a thin layer of cladding followed by a precision etch [39], but fabrication tolerances limit the depth of the window. Thick cladding, however, is critical to produce a large and symmetric mode well coupled to cleaved optical fiber. Here, we demonstrate a silicon nitride (SiN) fabrication process that allows for both waveguides with thick oxide cladding at the facet and waveguides without oxide cladding for diamond integration. As shown in Fig. 2, we employ a titanium-aluminum etch-stop layer directly on top of the SiN waveguides used for diamond integration, allowing a standard oxide etch to open a precision window in the top SiO_2 cladding without damaging the SiN layer (see Appendix B for details). The

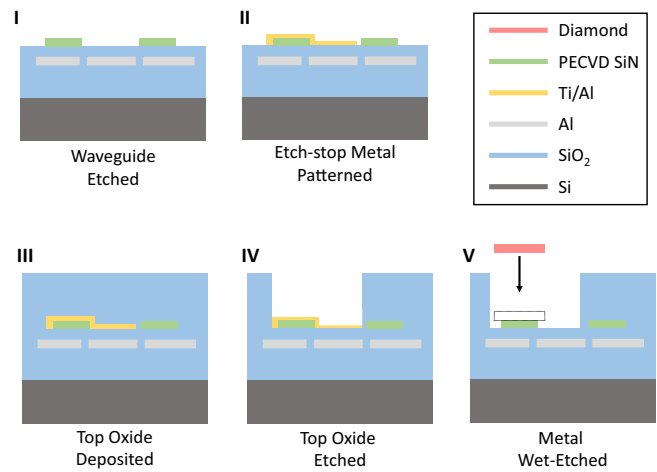


FIG. 2. Fabrication process steps relevant to the alternative PIC window opening, detailed in the text. Fully clad SiN waveguides allow for efficient mode overlap to standard single mode fiber, while a precision window etch provides for heterogeneous integration of a diamond microchiplet.

metal is then removed with a selective wet etch, and the resulting open window is shown in Fig. 3(a). The oxide-clad waveguides at the facet allows for a larger optical mode matched to cleaved optical fiber resulting in low-loss coupling to a 20-channel commercial fiber array with 630HP optical fiber.

The PIC is designed to support eight independent quantum emitter channels, based upon the eight independent diamond waveguides available on a single diamond microchiplet. SiN waveguides provide optical input (eight) and output (eight) access to the diamond using 16 total channels. To ease the integration of the PIC module with a commercial optical fiber array, the input and output SiN waveguides are routed to the same side of the PIC and spaced $127\ \mu\text{m}$ apart as shown in Fig. 7(a) of the Appendix. Two SiN waveguide loopback structures that are not routed through the diamond window are added

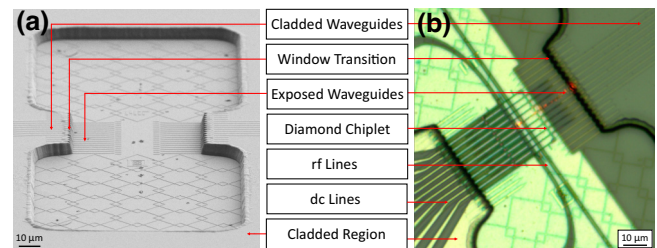


FIG. 3. The diamond window. (a) A scanning electron microscope image of the diamond window region with exposed SiN waveguides. (b) An optical image of a stamped diamond microchiplet onto the exposed SiN waveguides. Here you can see the alignment of the diamond waveguides as well as the microwave and dc electrical lines, which can be used to control the electronic states of the Si- V^- .

to the same PIC facet to help facilitate alignment with the fiber array and characterize alignment drift during packaging and cryocooling.

In addition to optical waveguides, metal electrodes are fabricated as part of the PIC module in a 0.75 μm -thick aluminum layer. The role of the electronic capabilities on the PIC is for future microwave control of the qubit and dc strain tuning of the diamond. Ground-signal-ground coplanar microwave waveguides are routed below the diamond window in order to deliver microwave control signals to the Si- V^- s. In addition, dc electrodes are patterned in the same aluminum layer and interdigitated with the individual diamond waveguides [see Fig. 7(c)] for future electrostatic actuation-based strain tuning [40] of the inhomogeneously spread color-center transition frequencies. For this work, microwave loss is measured but dc bias for strain tuning is not applied.

Attachment of the commercial fiber array to the custom PIC, while maintaining alignment from room temperature down below 100 mK, required the use of thermally compatible materials. We use a common silicon substrate and a silicon spacer—bonded with cryocompatible epoxy—to match vertical dimensions of the SiN waveguides on the PIC and the optical fibers in the fiber array as shown in Fig. 4. This majority-silicon design minimized relative motion between the fiber array and the PIC in the module during cooldown. We additionally apply UV epoxy in the interface between the fiber array and the PIC to eliminate any residual alignment drift. While we observe that UV epoxy alone is prone to failure at cryogenic temperatures, the added support from the cryocompatible epoxy is sufficient to maintain the UV epoxy bond and keep the module aligned. Our packaging procedure compares favorably to other methods (see, for example, Ref. [33]). Additional details for the packaging design and procedure are described in Appendix C.

After the module is fully cured, we place an eight-channel diamond chiplet onto the PIC [see Fig. 3(b)] using a custom-cut polydimethylsiloxane (PDMS) stamp affixed to a standard glass slide. We use a high-magnification zoom lens to image through the stamp to view the diamond chiplet and the PIC simultaneously and positioned the diamond chiplet with a six-axis stage with differential micrometers [41]. Correct diamond alignment with the SiN waveguides can be confirmed at room temperature using photoluminescence (PL, see Sec. III for details). Based on the submicrometer width of the SiN waveguides, we estimate a diamond placement accuracy of better than 100 nm, which compares very favorably with the approximately 10 μm placement accuracy inherent to commercially available pick-and-place systems. The module is then attached mechanically to a gold-plated copper puck and wire bonded to a custom-printed circuit board, as shown in Fig. 4. Custom fiber feedthroughs for up to 40 fibers (630HP)—supporting up to 16

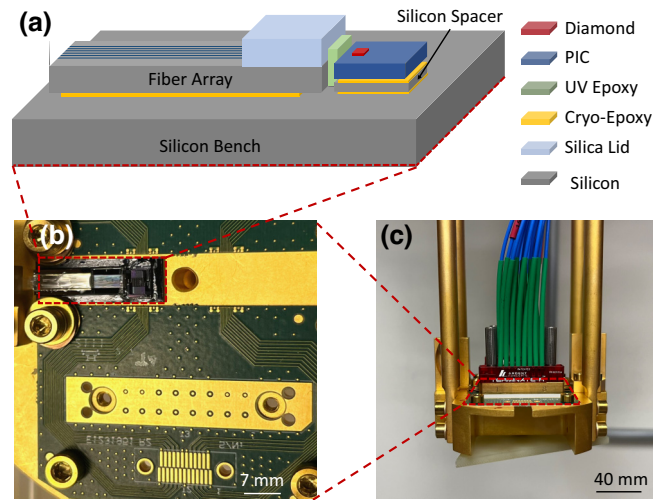


FIG. 4. Packaging details of the quantum emitter module. (a) The memory module is composed of a silicon bench, a silicon spacer, a silicon fiber array with a pyrex lid, and a silicon-on-insulator PIC. The elements are bonded with cryocompatible epoxy and UV epoxy is used in the interface. (b) The module is affixed to a gold-plated copper puck, wire bonded to a custom PCB, and (c) mounted in a dilution refrigerator with commercial microwave transmission cables.

diamond channels—through a single KF-40 flange and commercially available microwave and dc feedthroughs enabled operation of the module in our cryogenic system.

III. PERFORMANCE CHARACTERIZATION

We measure the optical and electrical properties of the quantum emitter module using the setup shown in Fig. 5. Light traveled from two laser sources at different wavelengths, combined at a 50:50 fiber splitter and combiner, through an optical fiber and down into a dilution refrigerator (DR). Excitation light is coupled into the module via one channel of a 20-channel fiber array, into the glued PIC and then transitioned from the PIC into the diamond chiplet, driving color centers to emit into the diamond waveguide mode. This fluorescence transitioned back into the PIC waveguide, into the fiber array and out of the DR where it is filtered spectrally and sent to either an avalanche photodiode (APD) for time-tagged photon detection, or a spectrometer for spectral characterization.

The figures of merit we consider for this architecture include the optical and microwave losses through the packaged system, the detected photon flux from the Si- V^- , and the linewidth of the Si- V^- emitters. We characterize the optical insertion loss of the PIC by using a short loop-back waveguide structure that does not pass through the diamond window on the PIC. We measure approximately 7-dB round-trip insertion loss at 737 nm, which included facet, propagation, and bend losses. Based upon measurements of test devices, we estimate the facet loss to be

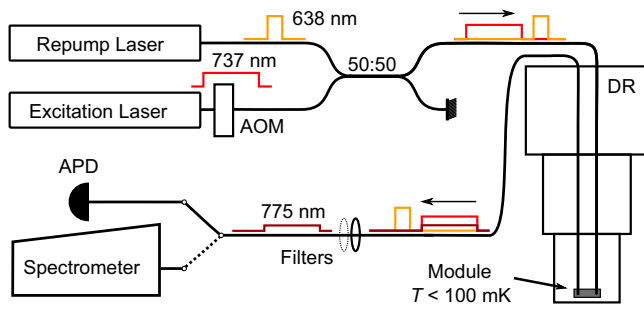


FIG. 5. Experimental setup. The resonant excitation laser light (red, 737 nm) is pulsed using an acousto-optic modulator (AOM), while the off-resonant repump laser (orange, 638 nm) is pulsed using current control. The resonant and off-resonant laser light is combined at a 50:50 fiber splitter and combiner and sent through custom fiber feedthroughs into the dilution refrigerator (DR). The light passes through the emitter module and then exits the DR with copropagating light from the phonon sideband (brown, 775 nm). The exiting light is filtered using a long-pass filter (LPF) that suppresses the the repump laser light and, optionally, a band-pass filter (BPF) that passes the phonon side band. After filtering, the optical signal is sent to a spectrometer to measure photoluminescence or to an avalanche photodiode (APD) to measure photoluminescent excitation.

approximately 3 dB/facet at 737 nm, which, crucially, is stable from room temperature down to 100 mK with no active alignment. This compares favorably to the room-temperature results of Ref. [42], which employs a bilayer SiN waveguide at 940 nm. The package is cycled from room temperature down below 100 mK multiple times with no appreciable change in transmission.

The fabricated PIC parameters are swept to explore the optimum geometry for these alternative structures and to reveal the most relevant fabrication limitations, which will inform future designs. Using cascaded test devices, our best performing window structures had approximately 3.0-dB loss per transition. This loss is primarily due to optical scattering as the waveguide passes directly through window etch, which we find to have a rough surface. This fabrication limitation can be overcome by moving to a design with a two-layer SiN stack and adiabatically transitioning between SiN layers within the window region. This would significantly reduce the window transition loss and would also allow for useful capabilities such as polarization control and low-loss optical routing. The best performing SiN-to-diamond transition devices resulted in 6.6-dB loss per transition. Loss in these devices arises from the SiN waveguide layer thickness—which is optimized for edge coupling performance between the PIC and the cleaved fiber array—resulting in imperfect mode matching between the SiN and diamond waveguides. This limitation can again be addressed by a two-layer SiN stack, where the bottom layer thickness is optimized for cleaved fiber to PIC transmission performance and the top layer thickness

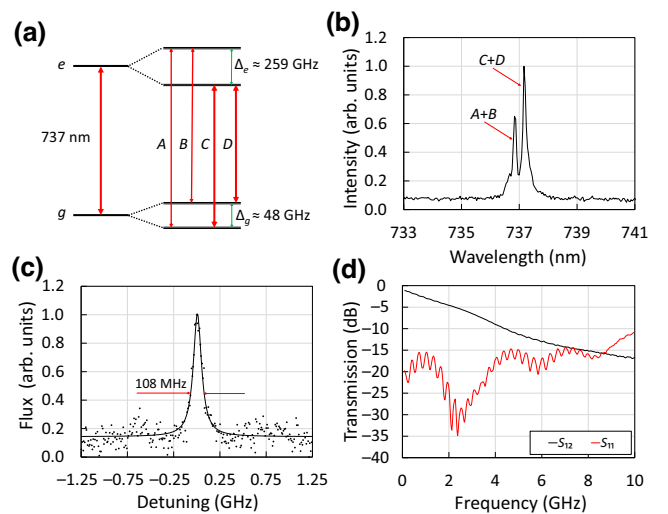


FIG. 6. Optical and electrical characterization. (a) The energy-level diagram of an Si- V^- color center with zero magnetic field. The excited state (e) and ground state (g) are split by spin-orbit coupling. The resulting manifold contains optical transitions (red lines) and microwave transitions (green lines). (b) A typical PL signal from an ensemble of color centers in a single waveguide using 638-nm excitation light with transitions labeled according to (a). (c) A high-resolution PLE scan of one Si- V^- using resonant 737- and 638-nm repump laser light and collecting the phonon sideband. Other channels are shown in Fig. 8 in the Appendix. (d) S parameters of the microwave transmission properties of an emitter module.

is optimized for SiN-to-diamond waveguide transmission. Finally, we estimate an optimum straight waveguide propagation loss of 0.30 dB/cm at 737 nm for 600-nm-wide waveguides, which could be improved by increasing the waveguide width from 600 nm up to 700 nm [43]. We note that there is increased loss near metals on the PIC, though this can be mitigated by moving the metal layer farther from the optical mode by increasing the oxide depth between the SiN and metal layer.

The microwave transmission through a typical module is shown in Fig. 6(d). This data is taken at room temperature, and we observe minimal changes in microwave transmission characteristics between room temperature and cryogenic operation. The data shows smooth transmission properties out to 10 GHz, indicating the module can deliver distortion-free microwave pulses to the Si- V^- color centers in the module, suitable for enabling quantum memory control operations [27]. The transmission loss is dominated by line loss from the cables, not by the module itself, which should result in minimal heating of the diamond microchiplet; preliminary results indicate that next-generation devices will be able to further reduce microwave loss for improved performance [44].

We demonstrate the functionality of our packaged module by performing optical spectroscopy of six color-center

emitters in separate diamond waveguides. The Si- V^- energy levels are shown in Figs. 6(a) and 6(b) shows a typical PL spectrum of an ensemble of color centers in a single waveguide under 638-nm excitation. For these measurements, we use cw light with approximately 5.2 μW of power in the diamond waveguide (calculated based upon known losses) and an integration time of 2 min with a background-subtracted count rate of 2.8 kHz. The output is filtered using a long-pass interference filter at 664 nm. The scan shows two 737-nm transitions due to the excited state splitting of the Si- V^- as shown Fig. 6(a). Similar results are found in all six transmitting waveguides.

To further explore the optical properties of the Si- V^- emitters, we take high-resolution photoluminescent excitation scans of six channels, finding similar results in each as shown in Appendix D. For these scans, we use the pulse sequence shown in Fig. 5 with optical powers that optimize the signal-to-noise ratio and linewidth of the emitter. To begin, the repump laser initializes the Si- V^- electronic state with a 500-ns pulse with a peak power of 4.1 μW in the diamond waveguide. After a period of 1.6 μs , a 10- μs resonant 737-nm pulse with a peak power of 440 pW in the diamond waveguide is applied to cycle the resonant transition. The optical power is calculated based upon known losses. Each full optical pulse cycle is 16.1 μs long and includes 10 μs of measurement time during the resonant pulse. The output light is filtered to collect the phonon sideband with two 46-nm bandpass filters centered at 775 nm. The resonant laser frequency is swept with emitted phonon sideband photon counts measured by an avalanche photodiode (APD) for many pulse cycles, ranging between 2.50×10^5 and 6.21×10^5 cycles, depending on the channel. A typical scan is shown in Fig. 6(c) with an individual Si- V^- resonance, including a Lorentzian fit with a full width at half maximum of 108 ± 11 MHz. These results confirm that the packaged module supports individual color-center characterization for future use in quantum memory applications.

IV. DISCUSSION AND OUTLOOK

In summary, we design, fabricate, package, and test a cryogenically compatible photonic quantum emitter module that has the potential to scale to many qubits. In particular, we have resolved two key issues for developing scalable memories for quantum networking—namely, a packaged optical interconnect that is both (a) temperature stable and (b) compatible with heterogeneous integration techniques, all while maintaining low loss at the PIC-to-fiber interface.

To put the efficiency of this quantum emitter module into context, the reported losses associated with successful networked quantum memory demonstrations ranges from tens of dB [45] to less than 1 dB [5]. This work provides an intermediate solution in terms of optical loss at 7 dB,

while also demonstrating a scalable architecture with multiple spatially separated emitters. Additionally, we think that the relatively straightforward modification of using a two-layer SiN stack to avoid window transition loss, and the incorporation of lensed fibers to reduce edge coupling loss, will result in a module with approximately 1 dB of loss.

By upgrading our cryogenic setup with a vector magnet to realize a long-lived spin qubit [27], and connecting the module to our Boston area quantum network testbed [46,47] we will be able to perform advanced system-level demonstrations across deployed fiber links. Furthermore, while we design and demonstrate this module's utility using Si- V^- color centers at 737 nm, by modifying its design wavelength our approach can be made compatible with a range of complementary technologies spanning the range of operation of silicon nitride, from the visible to the mid-IR band. This includes other color centers in diamond [48], defects in silicon carbide [49], and rare-earth ions implanted in various high index materials [50]. Additionally, the individual components and techniques developed here have use in enabling efficient alternative emitter characterization for quantum information processing use [44], and will likely be of significant benefit to interconnects between disparate technologies for quantum [51,52] and classical applications [53–55].

ACKNOWLEDGMENTS

Distribution Statement A. Approved for public release. Distribution is unlimited. This material is based upon work supported by the National Reconnaissance Office and the Under Secretary of Defense for Research and Engineering under Air Force Contract No. FA8702-15-D-0001. Any opinions, findings, conclusions or recommendations expressed in this material are those of the authors and do not necessarily reflect the views of the National Reconnaissance Office or the Under Secretary of Defense for Research and Engineering. © 2023 Massachusetts Institute of Technology. Delivered to the U.S. Government with Unlimited Rights, as defined in DFARS Part 252.227-7013 or 7014 (Feb 2014). Notwithstanding any copyright notice, U.S. Government rights in this work are defined by DFARS 252.227-7013 or DFARS 252.227-7014 as detailed above. Use of this work other than as specifically authorized by the U.S. Government may violate any copyrights that exist in this work.

This material is based upon work supported by the Center for Quantum Networks under NSF grant 1941583. M.S. acknowledges support from the NASA Space Technology Graduate Research Fellowship Program. Work performed on MIT campus is supported in part by the Air Force Office of Scientific Research under award number FA9550-20-1-0105, supervised by Dr. Gernot Pomrenke.

APPENDIX A: DIAMOND FABRICATION

The diamond microchiplet is fabricated using a similar process to the one shown in Refs. [26,37,38]. The fabrication process began with an electronic grade single-crystal diamond plate from Element 6. We perform plasma etching in Ar/Cl₂ followed by O₂ etching to remove 7 μm of the diamond surface in order to relieve strain in the sample. This is followed by ion implantation of ²⁹Si by Innovation Inc. with an effective areal dose of 10¹¹ ion/cm² at 175 keV for a mean depth of 115 nm. After implantation, the sample is annealed at 1200 °C in an ultrahigh vacuum furnace at 10⁻⁷ mbar, followed by cleaning in a boiling mixture of nitric acid, sulfuric acid, and perchloric acid (1:1:1) to remove any graphite formed during the anneal.

Once this implantation process is complete, diamond microchiplets are fabricated following the methods described in Ref. [37]. The chiplet is shown in Figs. 7(c) and 7(d). The diamond waveguides taper up linearly from approximately 50 to 320 nm over 3.0 μm. The eight diamond waveguides have a rectangular shape with a depth of 200 nm and are spaced as 3.0 μm. The resulting suspended microchiplet is then removed with a tungsten probe and placed (smooth-side-up) onto a custom polydimethylsiloxane (PDMS) stamp to transfer (smooth-side-down) to the SiN PIC, as described in Sec. II.

APPENDIX B: PIC FABRICATION

PICs are used to photonically access diamond color centers by routing optical signals at 628 and 737 nm from optical fiber, through SiN waveguides, and into a diamond microchiplet. These PICs are fabricated at wafer scale using MIT Lincoln Laboratory's 90-nm node 200-mm wafer foundry, using a SiN-on-SiO₂ plasma-enhanced chemical-vapor-deposition (PECVD) process [43].

For our devices, an aluminum layer (0.75 μm thickness) is deposited on SiO₂ for future microwave and dc control of Si-*V*⁻ color centers, followed by 1.5 μm of SiO₂ PECVD cladding. The oxide is then planarized via chemical-mechanical polishing to a total depth of 0.6 μm. A 100-nm-thick SiN layer is deposited and etched to form the optical waveguides. Due to the lack of a SiN-SiO₂ selective etch [56], we employ a titanium-aluminum (Ti-Al) etch-stop layer using a liftoff process. The etch-stop layer is deposited on top of selected SiN waveguides to aid in the removal of oxide cladding in regions where we employ diamond integration. This is followed by depositing 5 μm of SiO₂ and a standard masked oxide etch to open a window down to the etch-stop layer, followed by a wet etch that removes the Ti-Al etch stop layer, leaving the SiN layer underneath. Vias are patterned and etched to access the metal layer for wire bonding, and a 150-μm-deep and 100 μm-wide trench is used to define the dicing trenches

on four sides of the entire 4 × 5 mm PIC. An additional 500-μm-deep etch is done on the optical input facets of the PIC, resulting in a total etch depth at the facet of 650 μm. This enables the fiber array to come flush against the PIC facet during the bonding process. The resulting PICs had both clad and unclad SiN waveguides, high-quality edge facets and embedded microwave and dc electrodes. The fabrication steps relevant for opening the diamond window are shown in Fig. 2.

Photonic structures on the PIC module included linear inverted tapers, bends, and evanescent couplers to get the optical mode in and out of the diamond. This latter structure is composed of two parts: (a) a “window transition region” composed of a taper from the clad SiN waveguide to the unclad SiN waveguide in the open window region of the device; and (b) a “SiN-to-diamond transition” region composed of a linear taper from an unclad SiN waveguide into a diamond waveguide. The details are shown in Figs. 7(d) and 7(e). The window transition is accomplished by tapering the SiN waveguide from a 600 nm width in the clad region—section (i) in Fig. 7(e)—to a 1000 nm width in the unclad region—section (ii). During this taper, the window tapers open gradually over a distance of 5 μm—sections (ii) to (iii). The SiN-to-diamond transition is accomplished in the unclad window region, where the SiN waveguide is tapered down while the diamond waveguide is tapered up towards the desired width of 320 nm—section (iv). The optical mode is thus evanescently coupled from the 1000-nm-wide SiN waveguide to the diamond waveguide—section (v)—where it can interact with Si-*V*⁻ color centers. The losses of the window transition are measured to be 3.3 dB/transition using a variation of the cut-back method, where several back-to-back window transitions are nested together and the insertion loss over multiple window transitions is measured. The losses of the SiN-to-diamond transition are estimated to be 6.6 dB/transition by measuring total PIC insertion losses with diamond attached and back calculating the diamond transition losses from known insertion losses of all other components. A standard parameter sweep on separate test structures allowed identification of designs with lower losses, to be used as part of the full module design in future tape outs. We note that although Fig. 7(d) shows the layout of an ideal diamond placement onto the etched window, in practice, small angular displacements of the diamond microchiplet with respect to SiN waveguides resulting from manual diamond positioning could result in higher insertion losses.

Reasonable changes to the design and fabrication of these devices can offer significant improvements to the loss in the transition to the unclad SiN and from the unclad SiN waveguide to the diamond waveguide. These improvements can be accomplished by employing two layers of SiN and optimizing the layer thicknesses and taper parameters of the SiN and diamond waveguides.

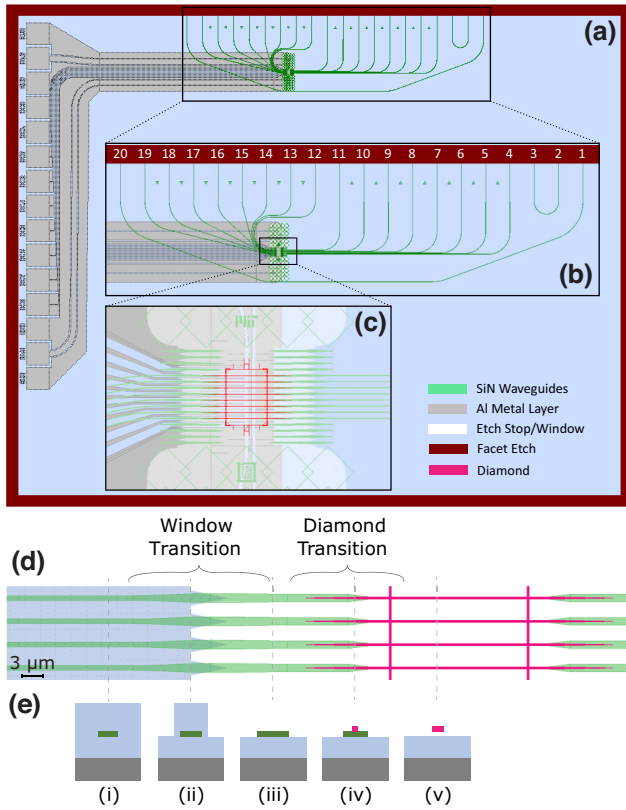


FIG. 7. PIC and diamond layout. (a) A layout of the full PIC with relevant structures, including two magnified insets. (b) The facets are shown with ten optical input and ten optical output channels. Channels 1, 2, 3, and 20 are used for optical alignment of the 20-channel fiber array, while channels 4–19 are used for diamond access. (c) The diamond integration region with diamond shown. (d) A magnified view of the window and diamond transition regions. (e) A cross-section view of (d), with regions (i)–(v) detailed in the text.

APPENDIX C: PACKAGING

As shown in Fig. 4, a 725- μm -thick silicon bench formed a common substrate for the PIC and fiber array; however, a 275- μm -thick silicon spacer between the silicon bench and the PIC is needed to allow clearance for the fiber core to align with the facet of the PIC. We design a custom jig to ensure precise alignment of the bench, spacer, and PIC. Using this jig, along with custom-cut spacers made from plastic shim stock, we are able to maintain a bond line of cryocompatible epoxy (MasterBond EP21TCHT-1) measuring approximately 76 μm for each layer. Pressure is applied with a Teflon-tipped screw from above for approximately 2 h to ensure that the PIC, spacer, and bench are parallel.

Before the epoxy is fully cured, we move the package to a bonding platform consisting of a three-axis translation stage and a custom-designed Delrin fixture to temporarily mount the PIC stack up. A commercial 20-channel silicon fiber array composed of 630HP single-mode fiber is

mounted to a six-axis translation stage with differential micrometers and a custom-fabricated rigid fixture. This fixture provided strain relief to the fibers and is able to release the fiber array after curing without disturbing the alignment. A high-magnification optical microscope with viewing camera is used to aid in bonding. Using a 730-nm diode laser with a polarization controller, we optimize alignment through loopback alignment structures on the PIC [see Fig. 7(b)], ensuring accurate alignment across the full length of the facet. Once aligned, the fiber array is raised out of the way and epoxy is applied to two regions: (a) the cryocompatible epoxy is applied to the silicon bench beneath the fiber array; (b) UV epoxy (Norland 63) is applied to the facet of the fiber array. The fiber array is then lowered back into position, forming a bond both below the array and between the array and the PIC. The alignment is optimized and then UV light is applied to the interface for approximately 60 min to ensure a complete cure. Compared to other methods [33], this bonding procedure is completed without the need for a temperature-controlled alignment stage. We allow the module to cure in the alignment setup for 24 h before transferring to a

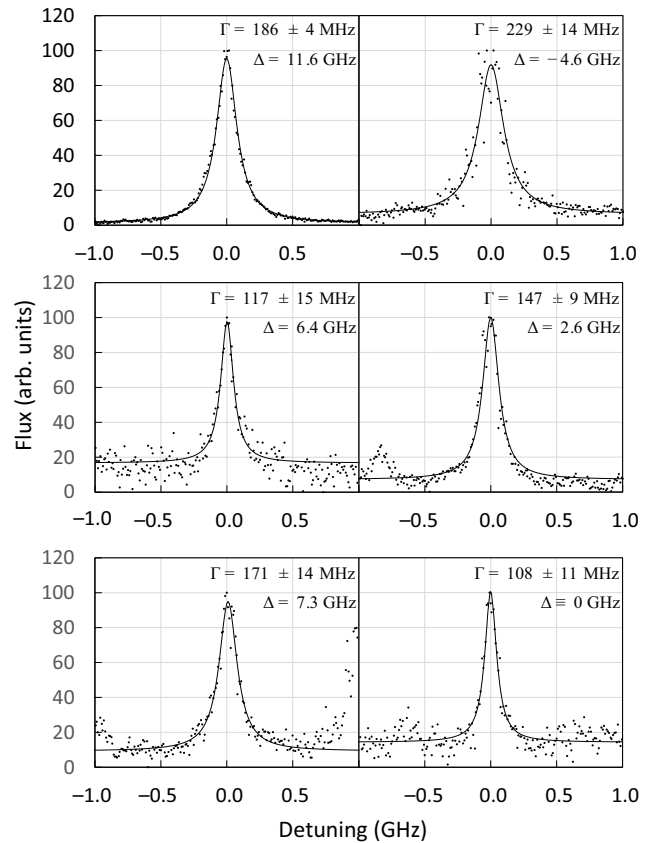


FIG. 8. Photoluminescent excitation (PLE) results. Six diamond channels are measured via the methods explained in the text. Lorentzian full width at half maximum Γ and the optical shift relative to the channel in Fig. 6(c) is shown.

dry box to complete the room-temperature cure of the cryocompatible epoxy over an additional 48 h.

APPENDIX D: OPTICAL CHARACTERIZATION

We measure PLE signals on six diamond channels as discussed in Sec. III. Data is taken using the methods discussed there, with integration times varied from 2.50 up to 6.20 s (2.50×10^5 – 6.21×10^5 cycles) to ensure adequate signal-to-noise based upon the brightness of the individual emitter. The results are shown in Fig. 8 with an arbitrary vertical axis. The Lorentzian full width at half maximum Γ as well as the shift in center frequency Δ relative to the Fig. 6(c) is shown. All emitters are within a 12-GHz range, and the linewidths vary from 108 up to 229 MHz.

-
- [1] S. Wehner, D. Elkouss, and R. Hanson, Quantum internet: A vision for the road ahead, *Science* **362**, 288 (2018).
- [2] H.-J. Briegel, W. Dür, J. I. Cirac, and P. Zoller, Quantum Repeaters: The Role of Imperfect Local Operations in Quantum Communication, *Phys. Rev. Lett.* **81**, 5932 (1998).
- [3] K. Azuma, S. E. Economou, D. Elkouss, P. Hilaire, L. Jiang, H.-K. Lo, and I. Tzitrin, Quantum repeaters: From quantum networks to the quantum internet (2022), [ArXiv:2212.10820](https://arxiv.org/abs/2212.10820).
- [4] W. J. Munro, K. A. Harrison, A. M. Stephens, S. J. Devit, and K. Nemoto, From quantum multiplexing to high-performance quantum networking, *Nat. Photonics* **4**, 792 (2010).
- [5] M. K. Bhaskar, R. Riedinger, B. Machielse, D. S. Levonian, C. T. Nguyen, E. N. Knall, H. Park, D. Englund, M. Lončar, and D. D. Sukachev, *et al.*, Experimental demonstration of memory-enhanced quantum communication, *Nature* **580**, 60 (2020).
- [6] P. Dhara, N. M. Linke, E. Waks, S. Guha, and K. P. Seshadreesan, Multiplexed quantum repeaters based on dual-species trapped-ion systems, *Phys. Rev. A* **105**, 022623 (2022).
- [7] Y. Lee, E. Bersin, A. Dahlberg, S. Wehner, and D. Englund, A quantum router architecture for high-fidelity entanglement flows in quantum networks, *Nat. Photonics* **8**, 75 (2022).
- [8] E. T. Khabiboulline, J. Borregaard, K. De Greve, and M. D. Lukin, Optical Interferometry with Quantum Networks, *Phys. Rev. Lett.* **123**, 070504 (2019).
- [9] C. Monroe, R. Raussendorf, A. Ruthven, K. R. Brown, P. Maunz, L.-M. Duan, and J. Kim, Large-scale modular quantum-computer architecture with atomic memory and photonic interconnects, *Phys. Rev. A* **89**, 022317 (2014).
- [10] D. Cuomo, M. Caleffi, and A. S. Cacciapuoti, Towards a distributed quantum computing ecosystem, *IET Quantum Commun.* **1**, 3 (2020).
- [11] B. C. Nichol, R. Srinivas, D. P. Nadlinger, P. Drmota, D. Main, G. Araneda, C. J. Ballance, and D. M. Lucas, An elementary quantum network of entangled optical atomic clocks, *Nature* **609**, 689 (2022).
- [12] V. Krutyanskiy, M. Galli, V. Krcmarsky, S. Baier, D. A. Fioretto, Y. Pu, A. Mazloom, P. Sekatski, M. Canteri, and M. Teller, *et al.*, Entanglement of Trapped-Ion Qubits Separated by 230 Meters, *Phys. Rev. Lett.* **130**, 050803 (2023).
- [13] S. Daiss, S. Langenfeld, S. Welte, E. Distanto, P. Thomas, L. Hartung, O. Morin, and G. Rempe, A quantum-logic gate between distant quantum-network modules, *Science* **371**, 614 (2021).
- [14] T. van Leent, M. Bock, F. Fertig, R. Garthoff, S. Eppelt, Y. Zhou, P. Malik, M. Seubert, T. Bauer, and W. Rosenfeld, *et al.*, Entangling single atoms over 33 km telecom fibre, *Nature* **607**, 69 (2022).
- [15] X.-Y. Luo, Y. Yu, J.-L. Liu, M.-Y. Zheng, C.-Y. Wang, B. Wang, J. Li, X. Jiang, X.-P. Xie, and Q. Zhang, *et al.*, Postselected Entanglement Between Two Atomic Ensembles Separated by 12.5 km, *Phys. Rev. Lett.* **129**, 050503 (2022).
- [16] Y. Wang, A. N. Craddock, R. Sekelsky, M. Flament, and M. Namazi, Field-Deployable Quantum Memory for Quantum Networking, *Phys. Rev. Appl.* **18**, 044058 (2022).
- [17] T. Zhong, J. M. Kindem, J. G. Bartholomew, J. Rochman, I. Craiciu, E. Miyazono, M. Bettinelli, E. Cavalli, V. Verma, and S. W. Nam, *et al.*, Nanophotonic rare-earth quantum memory with optically controlled retrieval, *Science* **357**, 1392 (2017).
- [18] D. Lago-Rivera, S. Grandi, J. V. Rakonjac, A. Seri, and H. de Riedmatten, Telecom-heralded entanglement between multimode solid-state quantum memories, *Nature* **594**, 37 (2021).
- [19] M. F. Askarani, A. Das, J. H. Davidson, G. C. Amaral, N. Sinclair, J. A. Slater, S. Marzban, C. W. Thiel, R. L. Cone, and D. Oblak, *et al.*, Long-Lived Solid-State Optical Memory for High-Rate Quantum Repeaters, *Phys. Rev. Lett.* **127**, 220502 (2021).
- [20] A. M. Dibos, M. Raha, C. M. Phenicie, and J. D. Thompson, Atomic Source of Single Photons in the Telecom Band, *Phys. Rev. Lett.* **120**, 243601 (2018).
- [21] J. M. Kindem, A. Ruskuc, J. G. Bartholomew, J. Rochman, Y. Q. Huan, and A. Faraon, Control and single-shot readout of an ion embedded in a nanophotonic cavity, *Nature* **580**, 201 (2020).
- [22] K. C. Miao, J. P. Blanton, C. P. Anderson, A. Bourassa, A. L. Crook, G. Wolfowicz, H. Abe, T. Ohshima, and D. D. Awschalom, Universal coherence protection in a solid-state spin qubit, *Science* **369**, 1493 (2020).
- [23] M. Ruf, N. H. Wan, H. Choi, D. Englund, and R. Hanson, Quantum networks based on color centers in diamond, *J. Appl. Phys.* **130**, 070901 (2021).
- [24] M. Pompili, S. L. N. Hermans, S. Baier, H. K. C. Beukers, P. C. Humphreys, R. N. Schouten, R. F. L. Vermeulen, M. J. Tiggelman, L. dos Santos Martins, and B. Dirkse, *et al.*, Realization of a multinode quantum network of remote solid-state qubits, *Science* **372**, 259 (2021).
- [25] A. J. Stolk, *et al.*, Telecom-Band Quantum Interference of Frequency-Converted Photons from Remote Detuned NV Centers, *PRX Quantum* **3**, 020359 (2022).
- [26] N. H. Wan, T.-J. Lu, K. C. Chen, M. P. Walsh, M. E. Trusheim, L. De Santis, E. A. Bersin, I. B. Harris, S. L. Mouradian, and I. R. Christen, *et al.*, Large-scale

- integration of artificial atoms in hybrid photonic circuits, *Nature* **583**, 226 (2020).
- [27] D. D. Sukachev, A. Sipahigil, C. T. Nguyen, M. K. Bhaskar, R. E. Evans, F. Jelezko, and M. D. Lukin, Silicon-Vacancy Spin Qubit in Diamond: A Quantum Memory Exceeding 10 ms with Single-Shot State Readout, *Phys. Rev. Lett.* **119**, 223602 (2017).
- [28] M. H. Abobeih, J. Cramer, M. A. Bakker, N. Kalb, M. Markham, D. J. Twitchen, and T. H. Taminiau, One-second coherence for a single electron spin coupled to a multi-qubit nuclear-spin environment, *Nat. Commun.* **9**, 2552 (2018).
- [29] C. E. Bradley, J. Randall, M. H. Abobeih, R. C. Berrevoets, M. J. Degen, M. A. Bakker, M. Markham, D. J. Twitchen, and T. H. Taminiau, A Ten-Qubit Solid-State Spin Register with Quantum Memory up to One Minute, *Phys. Rev. X* **9**, 031045 (2019).
- [30] P.-J. Stas, Y. Q. Huan, B. Machiels, E. N. Knall, A. Suleymanzade, B. Pingault, M. Sutula, S. W. Ding, C. M. Knaut, and D. R. Assumpcao, *et al.*, Robust multi-qubit quantum network node with integrated error detection, *Science* **378**, 557 (2022).
- [31] G. Waldherr, Y. Wang, S. Zaiser, M. Jamali, T. Schulte-Herbrüggen, H. Abe, T. Ohshima, J. Isoya, J. F. Du, and P. Neumann, *et al.*, Quantum error correction in a solid-state hybrid spin register, *Nature* **506**, 204 (2014).
- [32] R. J. Niffenegger, J. Stuart, C. Sorace-Agaskar, D. Kharas, S. Bramhavar, C. D. Bruzewicz, W. Loh, R. T. Maxson, R. McConnell, and D. Reens, *et al.*, Integrated multi-wavelength control of an ion qubit, *Nature* **586**, 538 (2020).
- [33] K. K. Mehta, C. Zhang, M. Malinowski, T.-L. Nguyen, M. Stadler, and J. P. Home, Integrated optical multi-ion quantum logic, *Nature* **586**, 533 (2020).
- [34] C. Cui, W. Horrocks, L. McCaffrey, V. Nafria, I. B. Djordjevic, and Z. Zhang, in *Conference on Lasers and Electro-Optics* (Optica Publishing Group, Virtual (online only), 2021), p. AM4O.5.
- [35] D. Du, P. Stankus, O.-P. Saira, M. Flament, S. Sagona-Stophel, M. Namazi, D. Katramatos, and E. Figueroa, An elementary 158 km long quantum network connecting room temperature quantum memories, *ArXiv:2101.12742* (2021).
- [36] J. Chung, E. M. Eastman, G. S. Kanter, K. Kapoor, N. Lauk, C. H. Peña, R. K. Plunkett, N. Sinclair, J. M. Thomas, and R. Valivarthi, *et al.*, Design and implementation of the Illinois express quantum metropolitan area network, *IEEE Trans. Quantum Eng.* **3**, 1 (2022).
- [37] S. Mouradian, N. H. Wan, T. Schröder, and D. Englund, Rectangular photonic crystal nanobeam cavities in bulk diamond, *Appl. Phys. Lett.* **111**, 021103 (2017).
- [38] N. H. Wan, S. Mouradian, and D. Englund, Two-dimensional photonic crystal slab nanocavities on bulk single-crystal diamond, *Appl. Phys. Lett.* **112**, 141102 (2018).
- [39] A. Chanana, H. Larocque, R. Moreira, J. Carolan, B. Guha, E. G. Melo, V. Anant, J. Song, D. Englund, and D. J. Blumenthal, *et al.*, Ultra-low loss quantum photonic circuits integrated with single quantum emitters, *Nat. Commun.* **13**, 7693 (2022).
- [40] S. Meesala, *et al.*, Strain engineering of the silicon-vacancy center in diamond, *Phys. Rev. B* **97**, 205444 (2018).
- [41] H. Raniwala, I. Christen, K. Chen, D. Starling, and D. Englund, Integrating nearly-indistinguishable quantum emitters onto a photonic interposer, in preparation (2023).
- [42] M. de Goede, H. Snijders, P. Venderbosch, B. Kassenberg, N. Kannan, D. H. Smith, C. Taballione, J. P. Epping, H. v. d. Vlekkert, and J. J. Renema, High fidelity 12-mode quantum photonic processor operating at InGaAs quantum dot wavelength (2022).
- [43] C. Sorace-Agaskar, D. Kharas, S. Yegnanarayanan, R. T. Maxson, G. N. West, W. Loh, S. Bramhavar, R. J. Ram, J. Chiaverini, and J. Sage, *et al.*, Versatile silicon nitride and alumina integrated photonic platforms for the ultraviolet to short-wave infrared, *IEEE. J. Sel. Top. Quantum Electron.* **25**, 1 (2019).
- [44] I. Christen, H. Raniwala, M. Colangelo, K. Chen, L. D. S. L. Li, Y. Song, C. Errando-Herranz, I. Harris, E. B. M. Sutula, and K. Berggren, *et al.*, in *Quantum 2.0 Conference and Exhibition* (Optica Publishing Group, Everett, Massachusetts, 2022), p. QM2A.4.
- [45] B. Hensen, H. Bernien, A. E. Dréau, A. Reiserer, N. Kalb, M. S. Blok, J. Ruitenber, R. F. L. Vermeulen, R. N. Schouten, and C. Abellán, *et al.*, Loophole-free bell inequality violation using electron spins separated by 1.3 kilometres, *Nature* **526**, 682 (2015).
- [46] E. Bersin, N. Wan, M. Bhaskar, D. Levonian, R. Riedinger, C. Langrock, M. M. Fejer, M. Lukin, P. B. Dixon, and S. Hamilton, *et al.*, in *Conference on Lasers and Electro-Optics* (Optica Publishing Group, Virtual (online only), 2021), p. AM4O.4.
- [47] D. Bunandar, A. Lentine, C. Lee, H. Cai, C. M. Long, N. Boynton, N. Martinez, C. DeRose, C. Chen, and M. Grein, *et al.*, Metropolitan Quantum Key Distribution with Silicon Photonics, *Phys. Rev. X* **8**, 021009 (2018).
- [48] M. E. Trusheim, B. Pingault, N. H. Wan, M. Gündoğan, L. De Santis, R. Debroux, D. Gangloff, C. Purser, K. C. Chen, and M. Walsh, *et al.*, Transform-Limited Photons from a Coherent Tin-Vacancy Spin in Diamond, *Phys. Rev. Lett.* **124**, 023602 (2020).
- [49] C. P. Anderson, E. O. Glen, C. Zeledon, A. Bourassa, Y. Jin, Y. Zhu, C. Vorwerk, A. L. Crook, H. Abe, and J. Ul-Hassan, *et al.*, Five-second coherence of a single spin with single-shot readout in silicon carbide, *Sci. Adv.* **8**, eabm5912 (2022).
- [50] P. Stevenson, C. M. Phenicie, I. Gray, S. P. Horvath, S. Welinski, A. M. Ferrenti, A. Ferrier, P. Goldner, S. Das, and R. Ramesh, *et al.*, Erbium-implanted materials for quantum communication applications, *Phys. Rev. B* **105**, 224106 (2022).
- [51] D. Awschalom, *et al.*, Development of Quantum Interconnects (QuICs) for Next-Generation Information Technologies, *PRX Quantum* **2**, 017002 (2021).
- [52] F. Najafi, J. Mower, N. C. Harris, F. Bellei, A. Dane, C. Lee, X. Hu, P. Kharel, F. Marsili, and S. Assefa, *et al.*, On-chip detection of non-classical light by scalable integration of single-photon detectors, *Nat. Commun.* **6**, 5873 (2015).
- [53] L. Stern, B. Desiatov, I. Goykhman, and U. Levy, Nanoscale light-matter interactions in atomic cladding waveguides, *Nat. Commun.* **4**, 1548 (2013).
- [54] A. Hermans, K. Van Gasse, J. O. Kjellman, C. Caër, T. Nakamura, Y. Inada, K. Hisada, T. Hirasawa, S. Cuyvers,

- and S. Kumari, *et al.*, High-pulse-energy iii-v-on-silicon-nitride mode-locked laser, *APL Photonics* **6**, 096102 (2021).
- [55] M. Chatzipetrou, *et al.*, A miniature bio-photonics companion diagnostics platform for reliable cancer treatment monitoring in blood fluids, *Sensors* **21**, 2230 (2021).
- [56] K. Williams, K. Gupta, and M. Wasilik, Etch rates for micromachining processing-Part II, *J. Microelectromech. Syst.* **12**, 761 (2003).